Thermodynamics of the Lu_2O_3 – SiO_2 system and comparison to other Rare Earth Silicates

Benjamin A. Kowalski, Nathan S. Jacobson, Cameron Bodenschatz, Gustavo Costa

NASA Glenn Research Center, 21000 Brookpark Road, Cleveland, OH, 44135, USA

Abstract

Environmental barrier coatings are necessary to protect SiC based ceramics and composites from water vapor degradation in harsh engine environments. Currently, rare earth (RE) silicates are the most promising systems to protect SiC based ceramics and composites. This protection is largely based on reduced silica activity in these rare earth silicates which results in a lowered reactivity with water vapor. To that end, previous Knudsen effusion mass spectrometry (KEMS) studies have explored RE = Yb, Y silicates to measure the reduced silica activity and subsequent water vapor reactivity. Similarly, this work employs the KEMS technique to measure the SiO(g) vapor pressure in Lu containing RE silicates to calculate the activity of silica within the monosilicate [$\log(a(SiO_2)) = -2351.1*1/T-1.6731$] and the disilicate ($\log(a(SiO_2)) = -4884.0*1/T + 2.2208$) as a function of temperature. The enthalpies of formation for Lu monosilicate from the oxides and the elements were calculated to be -45±3 kJ/mol at 1550 K and -2831.1±12 kJ/mol at 298 K, respectively. The measured enthalpy of formation and those found in literature are compared to modeled values from density functional theory and those estimated using electronegativity.

Introduction

SiC ceramics and composites are desired for use in high temperature applications because they allow for higher engine temperatures and therefore greater engine efficiency.[1] However, they are still susceptible to water vapor induced degradation. To protect against the harsh engine environment, an environmental barrier coating (EBC) is employed.[1] The EBC must meet a host of criteria, namely: a coefficient of thermal expansion of ~4-6*10^{-6}/K, good adhesion while remaining chemically compatible with the substrate, limit Ca-Mg-Al-Silicate (CMAS) glass infiltration and reactivity, and reduce water vapor induced volatilization all while usually at a density at or below 80-90%.[1–4] Currently, the rare earth

silicate (RES) materials have been identified as the most successful candidates for the protection of high temperature engine components due to matching most of the criteria described. As a note, the RE disilicates (REDS) match the criteria better than the RE monosilicates (REMS), but there is still sufficient interest in the REMS as possible candidate materials. As detailed by Opila *et al.,* SiO_2 volatility/reactivity is connected to activity and is incredibly important in these high temperature systems largely due to the chemical reaction in shown in Eq. (1).[5,6]

$$SiO_2(s) + 2H_2O(g) = Si(OH)_4(g) \quad (1)$$

The RES volatilize silica due to water vapor in a similar way, but at a rate largely reduced by the activity of the silica in the material. Because of this, experimental work abounds in literature on the water vapor induced volatility of the RES materials.[2,7–12] Opila and Jacobson have shown that the flux of $Si(OH)_4$ away from the material as described by a boundary layer limited gaseous diffusion model in a laminar flow situation can be represented Eq. (2).[5,13]

$$J_{Si(OH)_4} = 0.664 (\Re)^{0.5} (Sc)^{0.33} \frac{D_{Si(OH)_4}}{RTL} K a_{SiO_2} P_{H_2O}^2 \quad (2)$$

$$\Re = \frac{v_\infty \rho_\infty L}{\eta} \wedge Sc = \frac{\eta}{D_{Si(OH)_4} \rho_\infty}$$

where v_∞ is the free stream velocity, $\rho_\infty$is the free stream gas density, L is a characteristic dimension, η is the viscosity, R is the gas constant, T is the absolute temperature, and $D_{Si(OH)_4}$ is the gas phase diffusivity of $Si(OH)_4$, K is the equilibrium constant, a_{SiO_2} is the activity of SiO_2, and $P_{H_2O}$is the partial pressure of H_2O. In this formulation, the flux shows a clear dependence on the velocity ($v^{0.5}$), partial pressure of H_2O ($[P(H_2O)]^2$), and the activity of silica [$a(SiO_2)$] in the material. In a steam exposure experiment, the velocity and partial pressure of H_2O can be set and controlled. It is therefore necessary to measure the silica activity to complete the flux equation. In addition to this, some silicate materials, such as Lu silicate and Y silicate, experience both weight loss from volatilization and weight gain from contamination (i.e.

Al_2O_3) when tested in a steam environment due to the test setup itself. [8] This complicates verification of the material as a potential protective coating. Therefore, understanding the activity of the silicate material can help deconvolute the effects on weight change from multiple sources. To that end, silica activities will be obtained for both region (1) Lu_2O_3 + Lu_2SiO_5 and region (2) Lu_2SiO_5 + $Lu_2Si_2O_7$ shown in Fig 1. The activities will be compared to previous mass spectrometry experiments performed by Jacobson and Costa for Y_2O_3 and Yb_2O_3 containing silicates, respectively.[14,15]

In addition to calculating the activity, it is also of interest to determine the enthalpy of formation from the elements ($\Delta_f H^{el}$). In general, $\Delta_f H^{el}$ tends to become more negative with an increasing number of oxygen anions (*NA*) in the composition as shown in Fig. 2. This means that, for example, the $\Delta_f H^{el}$ of Mg_2SiO_4 (-2172 kJ/mol, *NA* = 4) is more negative than the $\Delta_f H^{el}$ of $MgSiO_3$ (-1549 kJ/mol, *NA* = 3) which are both more negative than the $\Delta_f H^{el}$ of MgO (-601.6 kJ/mol, *NA* = 1) or SiO_2 (-908.3 kJ/mol, *NA* = 2). It should also be noted that similar graphs could be drawn for other anions (i.e. carbon, fluorine, etc.), however, they would have a different slope. The data in Fig. 2 is taken from multiple sources and comprises binary, ternary, and quaternary oxides.[16–18] However, there is still spread in the $\Delta_f H^{el}$ data at each anion number indicating a reliance on other factors. Numerous studies have attempted to correlate thermodynamic properties to various parameters such as band gap, electronegativity, chemical hardness, and optical basicity to varying degrees of success.[15,19–21] This is indicative of an underlying connection between the crystal and electronic structures to both the activity and the $\Delta_f H^{el}$ as well as other thermodynamic properties.

As shown previously for Y and Yb monosilicate, the measured $\Delta_f H^{el}$ indicates greater stability vs their constituent oxides.[14,15] The $\Delta_f H^{el}$ of Lu monosilicate will be calculated in the same way. Subsequently, comparisons will be made between the measured $\Delta_f H^{el}$ of the Y, Yb, and Lu monosilicates and two theoretical determination methods. The first method provides modeled values from density functional theory (DFT). DFT provides a theoretical method for calculating the electronic structure of materials by solving the Kohn-Sham equation. Plane-wave DFT has successfully been used to calculate the

thermal and mechanical properties for a variety of rare-earth silicates.[22–25] The second method proposed by Zhuang estimates the $\Delta_f H^{el}$ using the electronegativities of the atoms involved.[21]

Experimental

Knudsen Effusion Mass Spectrometry system

The modified Nuclide type 12-HT-90 Knudsen effusion mass spectrometry (KEMS) system used in this work has been described in detail in previous articles, so only a brief description of the method used is provided here.[26] Similar to the previous studies, the KEMS setup used a three cell configuration with X-Y translation as shown in Fig. 3a that allowed for measurements of the vapor pressure of the effusates without the need for breaking vacuum between each sample. The orifice size of each Knudsen cell used is the same at 1.5 mm in diameter. Similarly, the inner diameter of each cell is the same at 1 cm in diameter. The amount of powder used in each cell is ~0.2-0.25 g. The powders have a particle size in the range of 1-2 μm. Therefore, near equilibrium can be reached between the condensed and vapor phases within the cell due to the sufficient ratio between the orifice size of the Knudsen cell and the high surface area of the loosely packed powder. Additionally, the concern of the orifice size of the Knudsen cell is mitigated by using collimating apertures (i.e. source and field apertures, Fig. 3a) to restrict the molecular beam which has been described in more detail by Chatillon and Copland.[26,27] Essentially, by using apertures with a size smaller than the Knudsen cell orifice size, only a well-defined angular range of molecules are permitted to enter the ion source to be ionized, allowing the ion source to effectively "see" into the Knudsen cell. This also limits errant molecules that did not originate from the Knudsen cell from entering the ionizer. The calibration of the instrument used in this work is described more fully by Copland.[26] The cells used to hold each mixture corresponded to the reducing agent used in the mixture which is described in Table 1, Figs. 3b & c, and the following paragraphs.

In this study, the partial pressures of the vapor species in the 1500 to 1750 K temperature range were measured with the KEMS system. The partial vapor pressure is calculated from the intensity of the effusate from the following equation:

$$P_i = \frac{k I_i T}{\sigma_i^E} (3)$$

where P_i is the partial pressure of species i, k is the instrument constant, I_i is the measured ion intensity for species i, T is the absolute temperature, and σ_i^E is the cross section of species i at a particular ionizing electron energy, E, which in this case is 26. Before a measurement, the temperature is allowed enough time to equilibrate, usually on the order of 30 min to 60 min. Additionally, 6 consecutive measurements are taken at each temperature to allow for calculation of the error in the measurement which is found to be less than 1%. The "measurements" presented throughout the work represent the averaged value of the 6 consecutive measurements.

Powder Preparation, Characterization, & Loading for Mass Spectrometry

The powders used in this study are described in Table 2. Lu_2SiO_5 was purchased from Alfa Aesar and $Lu_2Si_2O_7$ was prepared by conventional solid state processing. The disilicate composition was prepared as follows. Powders of Lu_2O_3 and SiO_2 were mixed in the stoichiometric amounts to produce $Lu_2Si_2O_7$. The powders were milled in ethanol for 24 h. After drying on a hot plate at 363 K, the powder was pressed into a 1" diameter x ½" thick disc. This disc was then placed in a Pt crucible and reactively sintered at 1853 K for 10 h in air. The pellet was subsequently crushed for use in mass spectrometry. X-ray diffraction (D8-Advance, Bruker) was used to determine phase purity in both the as-received and processed powders. XRD was also performed after the mass spectrometric measurement to understand any phase evolution that occurred due to possible reactions at elevated temperature. Subsequent analysis for phase identification was performed using High Score (Panalytical, Malvern) equipped with the International Centre for Diffraction Data (ICDD) Powder Diffraction File (PDF+, 2019).

The phase pure powders were then mixed and dry milled for 24 h in the stoichiometric amounts shown in Table 1 which correspond to the phase regions in the Lu_2O_3 - SiO_2 phase diagram shown in Fig 1.[28] Fig 3b shows the setup in the KEMS for when measuring in region (1) and Fig 3c shows the setup for measuring in region (2). The gold (Au) standard material is used for both temperature calibration from the melting point and vapor pressure calibration in both setups and contained in an Al_2O_3 cell. The Au calibration is used to calculate the instrument constant used in Eq. 3. Tantalum and molybdenum are used as reducing agents to effectively increase the SiO(g) signal without forming additional solid phases.[29] This method was developed for other systems, namely MnO-SiO_2, and allows for measurements at lower temperatures, closer to the regions of interest.[29] Further, the tantalum and molybdenum additions mean the cells can be made of these materials, simplifying the system and removing the concerns about sample/cell interactions. The chemical reactions with the respective reducing agents are listed in Table 1 for each region. The underline for the compound (comp) indicates a less than unit activity.

For region (1), the vapor pressures of TaO(g) and TaO_2(g) are calculated to be very small and hence neglected. Thus the method used in region (1) is to simply measure a vapor pressure of SiO(g) and determine the activity of SiO_2 (in solution) that would generate such a vapor pressure.[14,15,29] Essentially, the activity of SiO_2 in solution can be calculated by comparing the $\underline{P_{SiO}}$ calculated from the measured data using Eq. (3) to calibration curves of P_{SiO} determined from Ta-$SiO_{2,pure}$ in Factsage at each temperature. It should be noted that these activities are only approximate with large error bands due primarily to the conversion of ion intensity to vapor pressure and reliance on auxiliary calculations. In particular, in a much cited work on the study of inorganic systems with mass spectrometry, Drowart explains the importance of the cross section to the associated error in calculating the partial pressure.[30] Due to the difficulty in estimating the cross section, Drowart assumes the error to be between 5 to 20%, therefore 20% will be used in this work.In region (2), a more rigorous method was used which gives a better accuracy than the method used in region (1). Essentially, by using the two Knudsen cell setup (Mo:LDS:LMS & Mo:SiO_2) as shown in Fig. 3c, ratios can be taken of the intensities which negates the

need to estimate cross sections of the ionizing species. To allow for measurement of the high silica activity system at these temperatures and limit unwanted reaction products, molybdenum is used as the reducing agent even though it is less effective than tantalum. From the chemical equations for Mo(s) + $SiO_2(s)_{pure\ or\ comp}$ and Eq. (3) one can show that the equilibrium constants are equal such that:

$$K=\frac{\left[I^{\circ}(SiO)\right]^3 I^{\circ}[MoO_3]}{\left[a(SiO_{2,\,pure})\right]^3}=\frac{\left[I(SiO)\right]^3 I[MoO_3]}{\left[a(SiO_{2,\,comp})\right]^3} \quad (4)$$

For Mo-$SiO_{2,pure}$ the SiO_2 activity is taken as 1, which when rearranged, results in:

$$a(SiO_{2,\,comp})=\left\{\frac{\left[I(SiO)\right]^3 I[MoO_3]}{\left[I^{\circ}(SiO)\right]^3 I^{\circ}[MoO_3]}\right\}^{0.33} \quad (5)$$

DFT Computational Details

Plane-wave DFT using the projector-augmented wave (PAW) method as implemented in the Vienna Ab-initio Simulation Package (VASP) code was used to calculate the optimized structures and electronic energies.[31–34] The $2s^2 2p^4$, $3s^2 3p^2$, and $4s^2 4p^6 5s^1 4d^2$ electrons were treated as valence electrons for O, Si, and Y, respectively. Lu and Yb were considered to have a 3^+ oxidation state with $5p^6 6s^2 5d^1$ electrons treated as valence electrons; their 4*f* electrons were treated as core electrons. While the 4*f* electrons can be treated using more sophisticated methods such as GW_0 and DFT+*U* for electronic and optical property calculations, the structural and vibrational properties are adequately represented by the Lu^{3+}, and Yb^{3+} potentials.[35–37] For reference, the GW_0 approximation is used to calculate the self-energy of a many-body system using an expansion of the single-particle Green's function, G, and the screened coulomb interaction, W. Electronic exchange-correlation effects were treated using the Perdew-Burke-Ernzerhof revised for solids (PBEsol) functional form within the generalized gradient approximation (GGA).[38,39] In all DFT calculations, the plane-wave cutoff energy was 520 eV and the Brillouin zones were sampled using Γ-centered Monkhorst-Pack *k*-point meshes with a density of 1500 *k*-points per reciprocal atom.[40] Gaussian smearing with a smearing width of 0.05 eV was used. Electronic structures

were converged to a total energy tolerance of $1*10^{-8}$ eV and ionic structures were converged to a maximum ionic Hellmann-Feynman force tolerance of $1*10^{-4}$ eV/Å.

Phonon vibrational frequencies, free energies, and entropies were calculated as functions of temperature using the Phonopy package.[41] The second-order interatomic force constants were calculated using the finite-displacement method with 2x2x2 supercells.[42,43] Higher-order force constants were not calculated in this work due to their high computational expense. Phonon frequencies were calculated by iterating over the sampling *q*-mesh until the maximum difference in the corresponding calculated free energies between successive iterations at all temperature points was converged to less than $1*10^{-5}$ eV. Enthalpies were calculated as a function of temperature using $H \approx U = F + TS$, where *F* is the Helmholtz Free Energy, *T* is the temperature, and *S* is the entropy and the enthalpy, *H*, is approximated by the internal energy, *U*.

Results & Discussion

Region (1) – Lu_2O_3 + Lu_2SiO_5 + Ta

As expected from previous studies, region (1) had a low activity of silica.[14,15] However, unlike previous studies, appreciable tantalates were seen to form as shown in the XRD spectra in Fig. 4. Multiple runs were performed with fresh powder to understand the effect of the time on the tantalate formation. To illustrate this, Fig 5 shows a moving R^2 (linearity coefficient) as each new measurement is added to the set for a single run. From this representation, we can limit the data used for the determination of the activity and the enthalpy of formation to that taken before the tantalate formation begins to skew the measurement. Interestingly, this behavior lies in contrast to the Yb-Si-O-Ta system studied by Costa, where it was necessary to react the powders for 24 h beforehand to achieve equilibrium, but no secondary phases were formed.[15] Therefore, though Ta can still be used as a reducing agent, one must take care and approach each system differently.

The raw data for the Au temperature calibration and the SiO in region (1) are shown in the Van't Hoff plot in Fig. 6 as well as in supplemental table 1. From the slope of the ln(*IT*) Au plot, the heat of

vaporization can be determined as -346.7 kJ/mol which is close to the literature value of (-345.6 kJ/mol).[44] This indicates that the temperature calibration is correct, and that the measured vapor pressure of SiO can be considered correct as well with regards to temperature. From previous experiments, it was determined that total experimental error was within ~±5%.[14,15]

From Eq. (3) and the cross section of SiO using 4.42, the equilibrium pressure can be calculated.[45] It should be noted that Mann only provides atomic cross sections. The cross section of SiO was determined by an additive rule and the sum modified by a correction factor as has been done previously.[14,15] The equilibrium pressure is shown normalized to $P°$ (1 bar) such that $P = P^{meas}/P°$ vs 1/T in Fig. 7. As described earlier, it is possible to correlate the measured pressure to one calculated in Factsage for SiO as a function of temperature.[29] As expected the $a(SiO)_{meas}$ for Lu monosilicate (0.0006 at 1550K) is rather low in comparison to silica and is comparable to the other REMS (e.g. 0.0028 for YbMS at 1600K and 0.0005 for YMS at 1562K).[14,15] The $\log[a(SiO)_{meas}]$ is shown in Fig. 7 as a function of 1/T. Finally, from the slope of the $\log(a)$, the partial molar enthalpy of formation ($\Delta_f H^{ox}$) at 1550 K can be determined of the oxide reaction in Eq. (6).

$$SiO_{2(s,1550K)} + Lu_2O_{3(s,1550K)} = \left[Lu_2O_3 \cdot SiO_2\right]_{(s,1550K)} \quad (6)$$

$$\Delta_r H = \Delta_f H_{298}^{el,\prod} - \Delta_f H_{298}^{el,reac} \quad (7)$$

$$\Delta_r H = \Delta_f H_T^{ox} + \sum C_{p,i} \quad (8)$$

The $\Delta_f H^{ox}$ at 1550 K can be combined with the integrated heat capacities (C_p) of SiO_2, Lu_2O_3, and $Lu_2O_3{\cdot}SiO_2$ from 298 K to 1550 K and the $\Delta_f H^{el}$ at 298 K of SiO_2 and Lu_2O_3 to determine the $\Delta_f H^{el}$ at 298 K of $Lu_2O_3{\cdot}SiO_2$.[14,15] This is shown in equations (7) and (8) and in Table 3. An $\Delta_f H^{ox}$ for LuMS is found to be -45.0 ± 3 kJ/mol which compares to -99.6 ± 5 kJ/mol and -27 ± 2 kJ/mol for YMS and YbMS, respectively.[14,15] The thermodynamic cycle for the series of equations shown in Table 3 ultimately produces a value of -2831.1 kJ/mol for the $\Delta_f H^{el}$ of LuMS. This is a reasonable value given

that, from previous studies by Jacobson and Costa using this technique, it was found that YMS has a $\Delta_f H^{el}$ of -2907 kJ/mol and YbMS has a $\Delta_f H^{el}$ of -2774.1 kJ/mol.[14,15]

Region (2) – LuMS + LuDS + Mo

In region (2), since the silica activity is greater, Mo is used as the reducing agent instead of Ta in an attempt to avoid forming silicides and tantalates. Therefore, a Mo-SiO_2 reference cell can be used to determine the activity of silica similar to how data from Factsage was used for comparison in region (1) as described by Eqs. 4 and 5 in the experimental procedure. An Au containing Al_2O_3 cell is again used to determine the temperature during the measurements. The XRD spectra of the before and after of the powders are shown in Fig. 8 which show that no appreciable molybdates or silicides have formed.

The raw data, ln(*IT*) for the 3 cells is shown as a function of 1/T in Fig 9 as well as supplemental table 3. By applying Eq. (5) at each temperature, the activity of silica can be calculated using Eq. (5). This activity as a function of 1/T is shown in Fig. 10. The silica activity (~0.28) at 1760 K is similar to the activities for the previous systems studied.[14,15]

DFT Modeling of the Enthalpy of Formation

A comparison between the measured values and the modeled DFT is shown in Table 3. There is good agreement between the $\Delta_f H$ of the REMS from the elements at 298.15 K calculated from DFT (Lu: -2841.0, Yb: -2780.8, and Y: -2874.8) kJ/mol and the measured values (Lu: -2831.0, Yb: -2774.8, -2774.1 and Y: -2.868.5, -2907.1) kJ/mol.[14,15,46] However, deviations exist between the DFT and measured values for the $\Delta_f H^{ox}$ at high temperature (~13-64 kJ/mol) and the integrated heat capacities (~5-75 kJ/mol). These deviations could be due to the lack of higher order terms in the interatomic force constants, which are likely to deviate from quadratic behavior at high temperature.[47] However, these terms were not calculated in this work due to their high computational expense and the good agreement at 298.15 K with the simpler quadratic model. A quasi-harmonic approach incorporating anharmonicity is likely necessary

to increase accuracy at high temperature as thermal expansion makes a purely harmonic model insufficient.

Zhuang estimation of the Enthalpy of Formation

Zhuang *et al*. provides a method to predict the enthalpy of formation at 298.15K for double oxides from the elements from a combination of the enthalpies of formation ($\Delta_f H_A, \Delta_f H_B$) for the base oxides and the electronegativity of the elements which itself is an extension of work by Pauling.[21,48] The relevant equations for the $\Delta_f H^{el}$ and $\Delta_r H$ are reproduced here:

$$\Delta_f H^{el} = N_1 \Delta H^{\circ}_{f,A_mO_n} + N_2 \Delta H^{\circ}_{f,B_xO_y} + \Delta_r H \quad (9)$$

$$\Delta_r H = -F * x_1 * x_2 * Z * \left[\beta_A - \beta_B\right]^2 \quad (10)$$

where, N_1 and N_2 are the number of moles for A_mO_n and B_xO_y, respectively, x_1 and x_2 are the mole fractions, F is Faraday's constant(96.5 kJ/mol), Z is the sum (n+y) of the Oxygen in the two oxides irrespective of mol%, and β_A and β_B are the electronegativities of the elements A and B, respectively. The formulation of Eq. (9) is the same as that shown in Eq. (7) where the $\Delta_r H$ is the difference between the $\Delta_f H^{el}$ of the products and the reactants. The electronegativity of Si is taken as 1.9 with the REs having a range from 1.1 to 1.27.[49] For the lanthanide series, the electronegativity trends upwards with the decreasing ionic cation radii indicating that, from Eq. (10), the $\Delta_r H$ increases with either increasing cation radii or decreasing electronegativity as seen in Table 5. Ultimately, the trend in the $\Delta_r H$ for the lanthanide contraction is similar to that observed for other RE-containing oxide systems studied by Kanke & Navrotsky.[50]

The experimental and theoretical enthalpies of formation for the REMS are shown in Table 5. The predictions largely agree with work by Liang, Jacobson, Costa, and this study as seen in Table 5 where the % difference (%diff) between the modeled and the measured data is rather low. Therefore, it may then

be possible to use the method provided by Zhuang to allow for prediction of the $\Delta_f H^{el}$ of other REMS, and by extension, the REDS.

Volatilization in the Presence of Water Vapor

Jacobson, Costa, and Opila among others have shown previously that the volatilization of silica is highly reliant on the $a(SiO_2)$ as described in Eq. (2). Unfortunately, LuMS and LuDS tend to form aluminates in steam environments due to the presence of volatile species from the alumina tube. Therefore, it is difficult to decouple the weight gain from the aluminate and the weight loss from the volatilization of SiO.[8] However, using the activities determined with mass spectrometry it is still possible to calculate the flux of $Si(OH)_4$ away from the sample. The activities of the Lu, Yb, and Y monosilicates and disilicates and the calculated fluxes of $Si(OH)_4$ are shown in Table 4. The activities of the silicates are similar in scale and therefore, the resulting volatilization should be considered realistic.

Influence of Crystal structure

As one might expect, the crystal structure likely plays a role in the activity and consequently, the water vapor reactivity of the silica in the REMS, REDS and other silicate systems. Representative crystal structures are presented in Fig. 11. It is known that the water vapor volatilization proceeds along the path: REDS → REMS → RE_2O_3, where the silica is selectively volatilized.[51] The silica is arranged as tetrahedra in different configurations for the REDS and REMS structures. The REDS structure has a double island configuration of silica tetrahedra connected at one corner by a bridging oxygen, whereas in the REMS structure, the silica tetrahedra are arranged in an island configuration (i.e. completely isolated from each other.) As has been shown previously, the bridging oxygen is the first point of attack for forming $Si(OH)_4$ in the presence of water vapor for the double island configuration.[52] Therefore, it follows that the REMS structure would be less susceptible to water vapor attack due to the absence of the bridging oxygen.

The importance of an isolated silica tetrahedra is corroborated by Velbel on a study of the relative weathering rates of simple orthosilicates.[53] In this context, weathering is referring to the chemical and mechanical processes that can wear down materials which is analogous to the deleterious effect of water vapor. In the review, it was observed that the materials with the best weathering rates all had isolated silica tetrahedra. Velbel presented a persistence series for materials with isolated silica tetrahedra wherein Zircon had the best weathering rate and Olivine had the worst. However, all the materials in the persistence series have a greater silica volatilization rate than REMS or REDS.

The edge sharing between the silica tetrahedra and the non-Si cation polyhedra likely accounts for the increased volatilization in Zircon, Olivine, etc.[53] From Pauling's rules, stability from polyhedral interaction decreases along the following path: corner sharing → edge sharing → face sharing.[48] The instability, which can lead to structural distortions, is due to the central atoms in each polyhedra attempting to compensate for the increased electrostatic repulsions caused by the closer proximity. Therefore, it also likely that the arrangement of the silica and non-Si cation polyhedra play a role in the water vapor reactivity. Consequently, the REMS with smaller cation sizes like those that have been studied (e.g. Lu, Yb, Y, etc.) tend to have much more corner sharing than edge sharing of the silica tetrahedra to the RE polyhedra. Hence, in the search for better EBCs, it seems prudent to identify materials with crystal structures that have both isolated tetrahedra and corner sharing between the polyhedra, but with CTE's that are a more reasonable match for SiC.

Conclusions

EBC materials are needed to protect engine components for high temperature applications. The water vapor reactivity has been shown to be related to the thermodynamic activity of silica within in the material. To that end, this study measured the thermodynamic activity of SiO_2 in the two phase regions of the Lu_2O_3-SiO_2 system. The activities were calculated for the monosilicate ($\log(a(SiO_2)) = -2351.1*1/T-1.6731$) and the disilicate ($\log(a(SiO_2)) = -4884.0*1/T + 2.2208$) as a function of temperature. The activities were similar to previous studies on RE silicates. The $\Delta_f H^{ox}$ and $\Delta_f H^{el}$ of Lu monosilicate were

calculated to be -45±3 kJ/mol at 1550 K and -2831.1±12 kJ/mol at 298 K, respectively. The experimental values for the enthalpy of formation for the RE monosilicates were compared to modeling by DFT and estimation by Zhuang. For DFT, there is good agreement for the $\Delta_f H^{el}$, but deviations exist for the $\Delta_f H^{ox}$ and the heat capacities. This was attributed to the lack of higher order terms in the interatomic force constants, which are likely to deviate from quadratic behavior at high temperature. Finally, there is likely a link between the crystal structure and the resulting silica activity. This was attributed to the arrangement and linkage between the polyhedra in the silicate materials.

Acknowledgements

This work was funded under NASA's Transformative Aeronautics Concepts Program as a part of the Transformative Tools and Technologies Project. The authors declare that they have no conflict of interest.

Table 1: Mixtures describing phase regions in phase diagram for mass spectrometry.

Regions in phase diagram			Chemical reactions at temperature		
(1) Lu_2O_3 + Lu_2SiO_5	→	3Ta: 1Lu_2O_3: 1Lu_2SiO_5	2Ta(s) + 3SiO_2(s)$_{comp*}$	=	3SiO(g) + TaO + TaO_2(g)
(2) Lu_2SiO_5 + $Lu_2Si_2O_7$	→	3Mo: 1Lu_2SiO_5: 1$Lu_2Si_2O_7$	Mo(s) + 3SiO_2(s)$_{pure\ or\ comp*}$	=	3SiO(g) + MoO_3(g)

*Underline for compound (comp) indicates less than unit activity

Table 2: Starting materials

Powder	Source	Purity (wt%)*
Lu_2O_3	Alfa Aesar, Ward Hill, MA	99.9
SiO_2	Alfa Aesar, Ward Hill, MA	99.9
Lu_2SiO_5	Alfa Aesar, Ward Hill, MA	99.99
Ta	Alfa Aesar, Ward Hill, MA	99.97
Mo	Gallard Schlesinger, Carle Place, NY	99.95
Au	Alfa Aesar	99.99
$Lu_2Si_2O_7$	Synthesized in lab for this work	99

*Purity as stated by supplier except for $Lu_2Si_2O_7$ which was determined by X-ray Diffraction and XRD detection limits.

Table 3: Thermochemical steps to calculate $\Delta_f H^{el}$ of RE_2SiO_5 at 298 K for both the measured and DFT modeled data. The values for (5) and (6) in the DFT columns come from reference [17], otherwise if there is no reference next to the values, the data was measured or generated in this work. Uncertainty reported as one confidence interval.

			RE = Lu @ *T* = 1550K			**RE = Yb @ *T* = 1562K**			**RE = Y @ *T* = 1600K**		
			ΔH [kJ mol^{-1}], showing experimental data (Exp.) and modeled data (DFT)								
Reactants		**Products**	**Exp.**	**Ref.**	**DFT**	**Exp.**	**Ref.**	**DFT**	**Exp.**	**Ref.**	**DFT**
(1) $SiO_{2(s,\ T)}$ + $RE_2O_{3(s,T)}$	→	RE_2O_3•$(SiO_2)_{(s,\ T)}$	-45.0 ± 3		-74.0	-27.0 ± 2	[15]	-91.7	-99.6 ± 5	[14]	-86.5
(2) RE_2O_3•$(SiO_2)_{(s,\ T)}$	→	RE_2O_3•$(SiO_2)_{(s,\ 298K)}$	-251.2 ± 4	[28]	-214.1	-283.0 ± 3	[15]	-208.5	-253.4 ± 5	[14]	-229.2
(3) $RE_2O_{3(s,\ 298K)}$	→	$RE_2O_{3(s,\ T)}$	162.4 ± 5	[54]	149.3	165.2 ± 0.5	[15]	153.7	171.6 ± 4	[14]	143.1
(4) $SiO_{2(s,\ 298K)}$	→	$SiO_{2(s,\ T)}$	87.7 ± 4	[55]	82.7	87.9 ± 0.5	[15]	82.7	87.6 ± 4	[14]	82.7
(5) $2RE_{(s,\ 298K)}$ + $3/2O_{2(g,\ 298K)}$	→	$RE_2O_{3(s,\ 298K)}$	-1877.0 ± 8	[17]	-1877.0	-1809.0 ± 10	[17]	-1809.0	-1905.3 ± 10	[17]	-1905.3
(6) $Si_{(s,\ 298)}$ + $O_{2(g,\ 298K)}$	→	$SiO_{2(s,\ 298K)}$	-908.0 ± 2	[17]	-908.0	-908.0 ± 2	[17]	-908.0	-905.2 ± 10	[17]	-908.0
(1) + (2) + (3) + (4) + (5) + (6) = (7)											
(7) $Si_{(s,\ 298K)}$ +$2RE_{(s,\ 298K)}$ + $5/2O_{2(g,\ 298K)}$	→	RE_2O_3•$(SiO_2)_{(s,\ 298K)}$	-2831.1 ± 12		-2841.0	-2774.1 ± 11	[15]	-2780.8	-2907.0 ± 16	[14]	-2874.8

Table 4: Flux of $Si(OH)_4$ at 1773 K for various systems. Uncertainty reported as one confidence interval.

System	**Ref.**	**a(SiO_2)**	**Calculated Flux of $Si(OH)_4$ [mg·cm^{-2}·hr^{-1}]**
SiO_2		1	1.1E-2 ± 1.1E-3
Y_2SiO_5 + Y_2O_3	[14]	0.001 ± 1.8E-4	1.5E-5 ± 3.8E-6
Yb_2SiO_5 + Yb_2O_3	[15]	0.003 ± 5.4E-4	3.8E-5 ± 9.5E-6
Lu_2SiO_5 + Lu_2O_3		0.001 ± 2.0E-4	1.5E-5 ± 4.0E-6
Y_2SiO_5 + $Y_2Si_2O_7$	[14]	0.32 ± 1.7E-3	3.1E-3 ± 7.8E-4
Yb_2SiO_5 + $Yb_2Si_2O_7$	[15]	0.36 ± 1.9E-3	4.0E-3 ± 1.0E-3
Lu_2SiO_5 + $Lu_2Si_2O_7$		0.29 ± 1.5E-3	3.2E-3 ± 8.0E-4

Table 5: RE_2SiO_5 Δ_fH^{el}: RE + Si + O based on Zhuang estimation [21]. Uncertainty reported as one confidence interval.

RE_2O_3	β*	RE_2O_3 Δ_fH [kJ/mol] [17]		SiO_2 Δ_fH [kJ/mol] [17]		Δ_rH calc. [kJ/mol]		RE_2SiO_5 Δ_fH^{el} est. [kJ/mol]	RE_2SiO_5 Δ_fH^{el} exp. [kJ/mol]	$\%Diff_{est.\ vs\ meas.}$
Y	1.22	-1905.0 ± 10	+	-908 ± 2	+	-55.8	=	-2868.8	-2868.5 [25], -2907.1 [24]	0.01, 1.3
La	1.1	-1791.6 ± 1	+	-908 ± 2	+	-77.2	=	-2776.8		
Ce	1.12	-1799.8 ± 2	+	-908 ± 2	+	-73.4	=	-2781.2		
Pr	1.13	-1809.9 ± 3	+	-908 ± 2	+	-71.5	=	-2789.4		
Nd	1.14	-1806.9 ± 3	+	-908 ± 2	+	-69.7	=	-2784.6		
Pm†	1.13	-1811.0 ± 21	+	-908 ± 2	+	-71.5	=	-2790.5		
Sm	1.17	-1826.8 ± 4	+	-908 ± 2	+	-64.3	=	-2799.1		
Gd	1.2	-1819.7 ± 4	+	-908 ± 2	+	-59.1	=	-2786.8		
Tb	1.22	-1865.2 ± 6	+	-908 ± 2	+	-55.8	=	-2829.0		
Dy	1.22	-1863.4 ± 5	+	-908 ± 2	+	-55.8	=	-2827.2		
Ho	1.23	-1883.3 ± 8	+	-908 ± 2	+	-54.2	=	-2845.5		
Er	1.24	-1900.1 ± 7	+	-908 ± 2	+	-52.5	=	-2860.6		
Yb	1.26	-1814.5 ± 6	+	-908 ± 2	+	-49.4	=	-2771.9	-2774.8 [25], -2774.1 [15]	-0.1, -0.08
Lu	1.27	-1877.0 ± 8	+	-908 ± 2	+	-47.9	=	-2832.9	-2831.1	0.06

*β: Electronegativity, β(Yb) taken as the linear interpolation between β(Th) and β(Lu). †Δ_fH of Pm_2O_3 found in Konings [56].

-

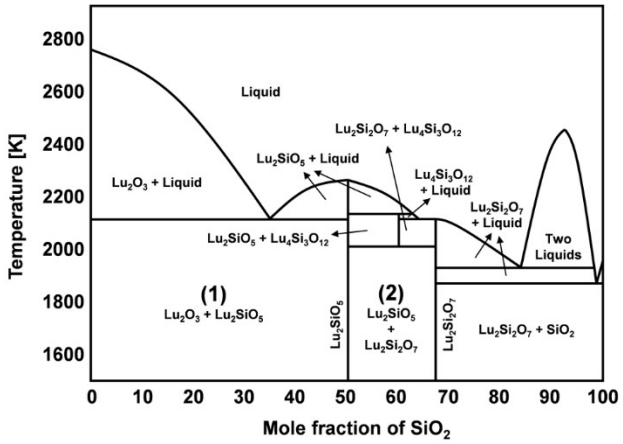

Figure 1: Phase diagram of Lu_2SiO_3 – SiO_2. Lu_2SiO_5 and $Lu_2Si_2O_7$ at 50 and 66 SiO_2 mole fraction, respectively. Region (1) and Region (2) investigated in this study are marked. Phase diagram reproduced after Ye (2017)

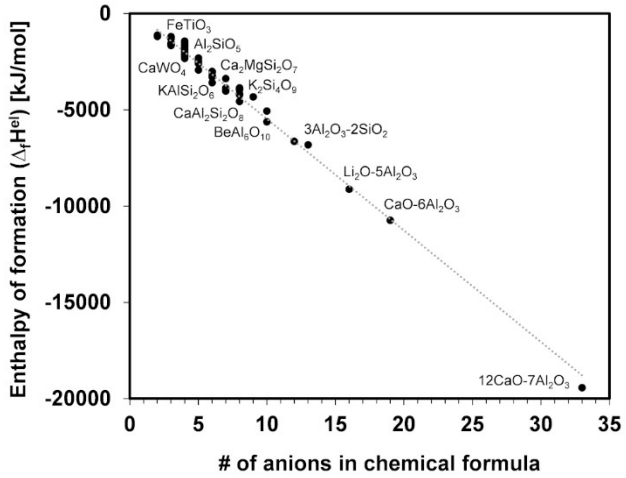

Figure 2: Enthalpy of formation from the elements versus the number of anions (i.e. Oxygen) in the chemical formula. Linear relationship due to the additivity of the enthalpy.

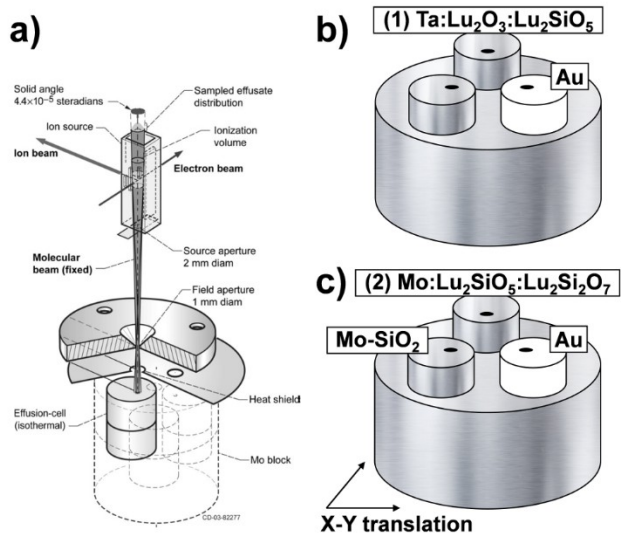

Figure 3: (a) Knudsen Effusion Mass Spectrometry system. (b) 3 cell setup for Region (1) and (c) 3 cell setup for Region (2)

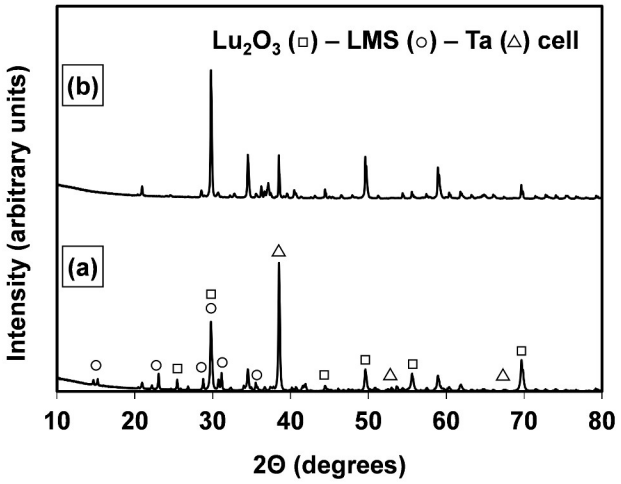

Figure 4: X-ray diffraction spectra of Region (1) powder (a) as mixed and (b) after mass spectrometry measurements.

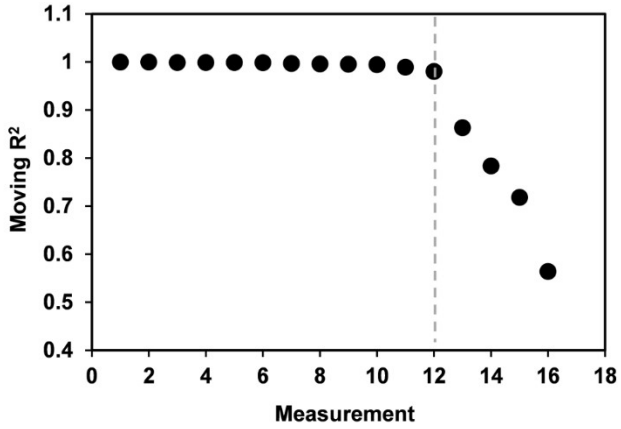

Figure 5: Moving R^2 (linearity coefficient) as each measurement is added to the set for Region (1). Measurements used for the calculation of the $\Delta_f H$ are taken from the measurement 1 to the dashed line.

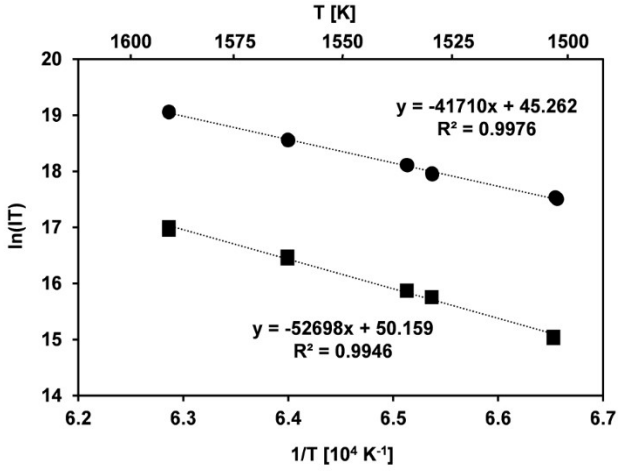

Figure 6: Dependence of ln(IT) vs 1/T for SiO in Region (1) Ta-Lu_2O_3-LMS (squares) and Au calibration (circles).

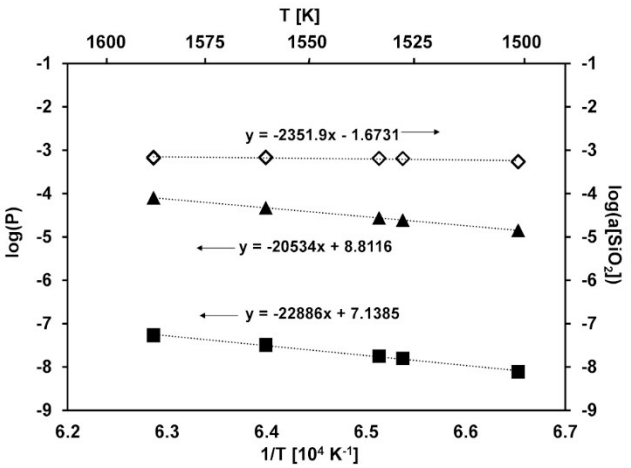

Figure 7: Dependence of log(P) vs 1/T for SiO in Region (1) Ta-Lu_2O_3-LMS (filled squares), SiO from Factsage (filled triangles). Combining the measured data with the modeled Factsage data allows the plotting of the dependence of log(a[SiO2]) vs 1/T (empty diamonds). Arrows indicate the corresponding y-axis.

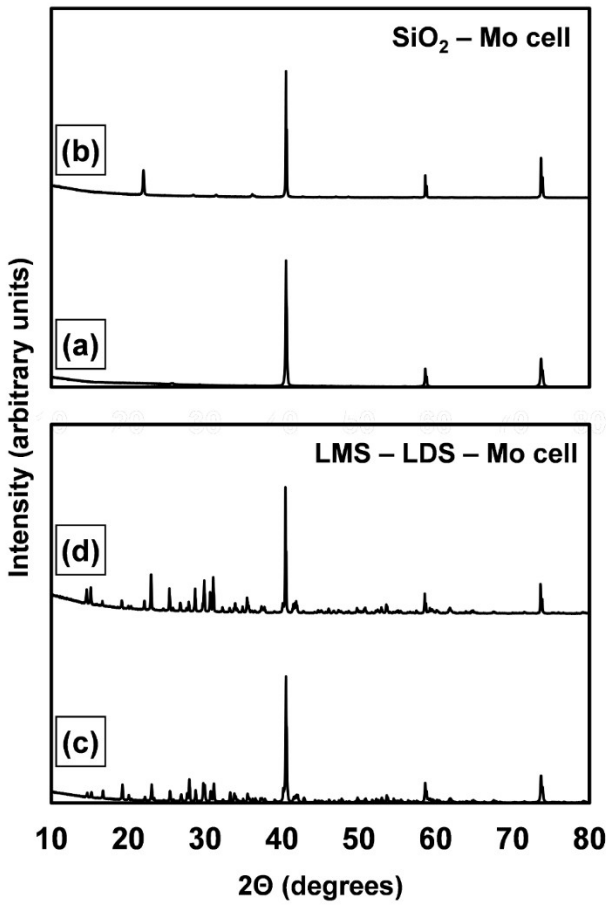

Figure 8: X-ray diffraction spectra of SiO_2 – Mo powder (a) as mixed and (b) after KEMS measurement. X-ray diffraction spectra of Region (2) LMS – LDS – Mo powder (c) as mixed and (d) after KEMS measurement.

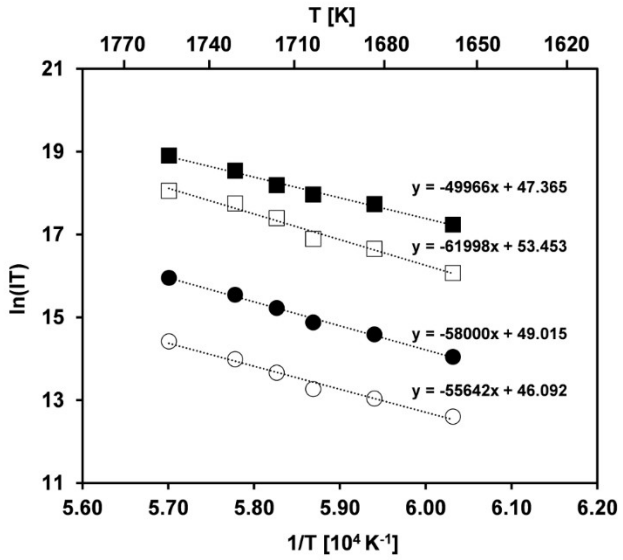

Figure 9: Dependence of ln(IT) vs 1/T for SiO and MoO_3 in both Region (2) LMS-LDS-Mo and SiO_2-Mo. SiO and MoO_3 are represented by squares and circles, respectively. Furthermore, LMS-LDS-Mo and SiO_2 are represented by open and close shapes, respectively.

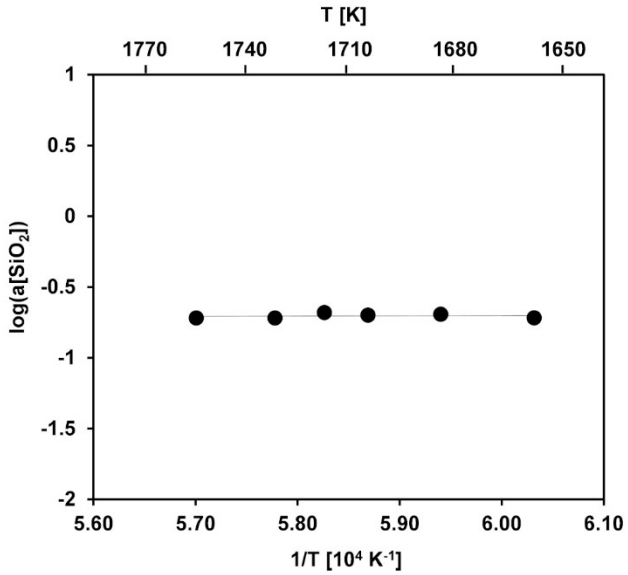

Figure 10: Dependence of log(a[SiO_2]) vs 1/T for Region (2) LMS-LDS-Mo as calculated from the data in Fig. 8 and Eq. (5).

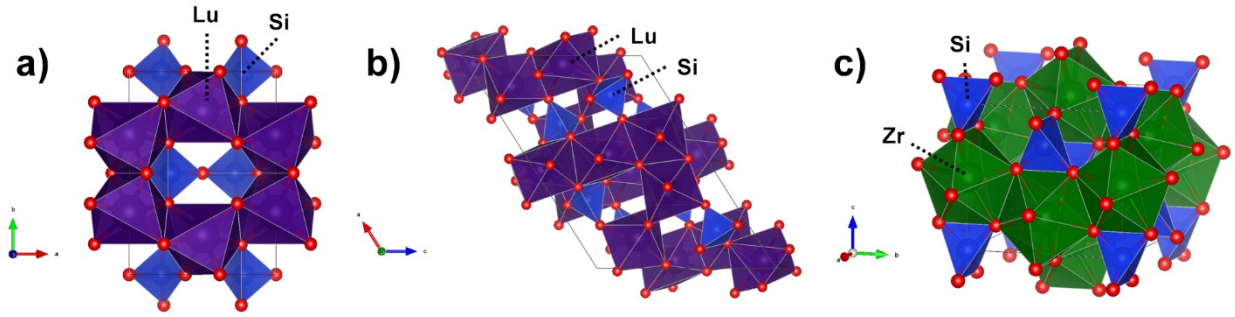

Figure 11: Crystal structures of a) $Lu_2Si_2O_7$, b) Lu_2SiO_5 c) $ZrSiO_4$. Images generated with VESTA

References

[1] K.N. Lee, N.S. Jacobson, R.A. Miller, Refractory oxide coatings on SiC ceramics, MRS Bull. 19 (1994) 35–38. https://doi.org/10.1557/S088376940004820X.

[2] N.S. Jacobson, D.S. Fox, J.L. Smialek, E.J. Opila, C. Dellacorte, K.N. Lee, Performance of ceramics in severe environments, Corros. Mater. 5245 (2018) 565–578. https://doi.org/10.31399/asm.hb.v13b.a0003842.

[3] Y. Song, S. Dhar, L.C. Feldman, G. Chung, J.R. Williams, Modified Deal Grove model for the thermal oxidation of silicon carbide, J. Appl. Phys. 95 (2004) 4953–4957. https://doi.org/10.1063/1.1690097.

[4] V.L. Wiesner, N.P. Bansal, Mechanical and thermal properties of calcium – magnesium aluminosilicate, J. Eur. Ceram. Soc. 35 (2015) 2907–2914. https://doi.org/10.1016/j.jeurceramsoc.2015.03.032.

[5] E.J. Opila, R.E. Hann, Paralinear oxidation of CVD SiC in water vapor, J. Am. Ceram. Soc. 80 (1997) 197–205. https://doi.org/10.1111/j.1151-2916.1997.tb02810.x.

[6] N.S. Jacobson, E.J. Opila, D.L. Myers, E.H. Copland, Thermodynamics of gas phase species in the Si-O-H system, J. Chem. Thermodyn. 37 (2005) 1130–1137. https://doi.org/10.1016/j.jct.2005.02.001.

[7] N. Al Nasiri, N. Patra, D.D. Jayaseelan, W.E. Lee, Water vapour corrosion of rare earth monosilicates for environmental barrier coating application, Ceram. Int. 43 (2017) 7393–7400. https://doi.org/10.1016/j.ceramint.2017.02.123.

[8] K.N. Lee, D.S. Fox, N.P. Bansal, Rare earth silicate environmental barrier coatings for SiC/SiC composites and Si_3N_4 ceramics, J. Eur. Ceram. Soc. 25 (2005) 1705–1715. https://doi.org/http://dx.doi.org/10.1016/j.jeurceramsoc.2004.12.013.

[9] A. V. Fedkin, L. Grossman, M.S. Ghiorso, Vapor pressures and evaporation coefficients for melts of ferromagnesian chondrule-like compositions, Geochim. Cosmochim. Acta. 70 (2006) 206–223. https://doi.org/10.1016/j.gca.2005.08.014.

[10] K.N. Lee, Current status of environmental barrier coatings for Si-based ceramics, Surf. Coatings Technol. 133–134 (2000) 1–7. https://doi.org/10.1016/S0257-8972(00)00889-6.

[11] S. Ueno, T. Ohji, H.T. Lin, Designing lutetium silicate environmental barrier coatings for silicon nitride and its recession behavior in steam jets, J. Ceram. Process. Res. 7 (2006) 20–23.

[12] B.T. Richards, K.A. Young, F. de Francqueville, S. Sehr, M.R. Begley, H.N.G. Wadley, Response of ytterbium disilicate–silicon environmental barrier coatings to thermal cycling in water vapor, Acta Mater. 106 (2016) 1–14. https://doi.org/10.1016/j.actamat.2015.12.053.

[13] N.S. Jacobson, M.A. Kuczmarski, B.A. Kowalski, Vaporization of protective oxide films into different gas atmospheres, Oxid. Met. 93 (2020) 247–282. https://doi.org/10.1007/s11085-019-09921-1.

[14] N.S. Jacobson, Silica Activity Measurements in the Y2O3–SiO2 System and Applications to Modeling of Coating Volatility, J. Am. Ceram. Soc. 97 (2014) 1959–1965. https://doi.org/10.1111/jace.12974.

[15] G.C.C. Costa, N.S. Jacobson, Mass spectrometric measurements of the silica activity in the Yb2O3-SiO2 system and implications to assess the degradation of silicate-based coatings in

combustion environments, J. Eur. Ceram. Soc. 35 (2015) 4259–4267. https://doi.org/10.1016/j.jeurceramsoc.2015.07.019.

[16] M. V. Shtenberg, V.A. Bychinskii, O.N. Koroleva, N.M. Korobatova, A.A. Tupitsyn, S. V. Fomichev, V.A. Krenev, Calculation of the formation enthalpies, standard entropies, and standard heat capacities of alkali and alkaline-earth germanates, Russ. J. Inorg. Chem. 62 (2017) 1464–1468. https://doi.org/10.1134/S0036023617110183.

[17] A. Navrotsky, W. Lee, A. Mielewczyk-Gryn, S. V. Ushakov, A. Anderko, H. Wu, R.E. Riman, Thermodynamics of solid phases containing rare earth oxides, J. Chem. Thermodyn. 88 (2015) 126–141. https://doi.org/10.1016/j.jct.2015.04.008.

[18] R. Robie, D. Waldbaum, Thermodynamic properties of minerals and related substances at 298.15 K and 1 bar (10^5 pascals) pressure and at higher temperatures, 1995. https://doi.org/10.3133/b2131.

[19] J. Portier, H.S. Hilal, I. Saadeddin, S.J. Hwang, M.A. Subramanian, G. Campet, Thermodynamic correlations and band gap calculations in metal oxides, Prog. Solid State Chem. 32 (2004) 207–217. https://doi.org/10.1016/j.progsolidstchem.2005.05.001.

[20] S.F. Matar, G. Campet, M.A. Subramanian, Electronic properties of oxides: Chemical and theoretical approaches, Prog. Solid State Chem. 39 (2011) 70–95. https://doi.org/10.1016/j.progsolidstchem.2011.04.002.

[21] W. Zhuang, J. Liang, Z. Qiao, J. Shen, Y. Shi, G. Rao, Estimation of the standard enthalpy of formation of double oxide, J. Alloys Compd. 267 (1998) 6–10. https://doi.org/10.1016/S0925-8388(97)00570-7.

[22] Y. Luo, L. Sun, J. Wang, Z. Wu, X. Lv, J. Wang, Material-genome perspective towards tunable thermal expansion of rare-earth di-silicates, J. Eur. Ceram. Soc. 38 (2018) 3547–3554. https://doi.org/10.1016/j.jeurceramsoc.2018.04.021.

[23] Z. Tian, L. Zheng, Z. Li, J. Li, J. Wang, Exploration of the low thermal conductivities of γ-Y2Si2O7, β-Y2Si2O7, β-Yb2Si2O7, and β-Lu2Si2O7 as novel environmental barrier coating candidates, J. Eur. Ceram. Soc. 36 (2016) 2813–2823. https://doi.org/10.1016/j.jeurceramsoc.2016.04.022.

[24] H. Xiang, Z. Feng, Y. Zhou, Mechanical and thermal properties of Yb 2 SiO 5 : First-principles calculations and chemical bond theory investigations, J. Mater. Res. 29 (2014) 1609–1619. https://doi.org/10.1557/jmr.2014.201.

[25] Z. Ding, M. Ridley, J. Deijkers, N. Liu, M.S. Bin Hoque, J. Gaskins, M. Zebarjadi, P. Hopkins, H. Wadley, E. Opila, K. Esfarjani, The physical and mechanical properties of hafnium orthosilicate: experiments and first-principles calculations, Preprint. (2020). http://arxiv.org/abs/2003.07546.

[26] E.H. Copland, N.S. Jacobson, Measuring Thermodynamic Properties of Metals and Alloys With Knudsen Effusion Mass Spectrometry, (2010) 1–54. https://doi.org/10.1002/9781118180730.ch48.

[27] C. Chatillon, L.F. Malheiros, P. Rocabois, M. Jeymond, High-temperature mass spectrometry with the Knudsen cell: II. Technical constraints in the multiple-cell method for activity determinations, High Temp. - High Press. 34 (2002) 213–233. https://doi.org/10.1068/htjr021.

[28] X. Ye, Y. Luo, S. Liu, D. Wu, D. Hou, F. Yang, Experimental study and thermodynamic calculation of Lu2O3-SiO2 binary system, J. Rare Earths. 35 (2017) 927–933. https://doi.org/10.1016/S1002-0721(17)60996-7.

[29] A.I. Zaitsev, B.M. Mogutnov, Thermodynamic Properties and Phase Equilibria in the MnO-SiO2 System, J. Chem. Soc. Faraday Trans. (1995) 1063–1073. https://doi.org/10.1039/FT9959100703.

[30] J. Drowart, P. Goldfinger, Investigation of Inorganic Systems at High Temperature by Mass Spectrometry, Angew. Chemie Int. Ed. English. 6 (1967) 581–596. https://doi.org/10.1002/anie.196705811.

[31] P.E. Blöchl, Projector augmented-wave method, Phys. Rev. B. 50 (1994) 17953–17979. https://doi.org/10.1103/PhysRevB.50.17953.

[32] G. Kresse, J. Furthmüller, Efficient iterative schemes for ab initio total-energy calculations using a plane-wave basis set, Phys. Rev. B. 54 (1996) 11169–11186. https://doi.org/10.1103/PhysRevB.54.11169.

[33] G. Kresse, J. Furthmüller, Efficiency of ab-initio total energy calculations for metals and semiconductors using a plane-wave basis set, Comput. Mater. Sci. 6 (1996) 15–50. https://doi.org/10.1016/0927-0256(96)00008-0.

[34] G. Kresse, D. Joubert, From ultrasoft pseudopotentials to the projector augmented-wave method, Phys. Rev. B. 59 (1999) 1758–1775. https://doi.org/10.1103/PhysRevB.59.1758.

[35] H. Jiang, P. Rinke, M. Scheffler, Electronic properties of lanthanide oxides from the GW perspective, Phys. Rev. B. 86 (2012) 125115. https://doi.org/10.1103/PhysRevB.86.125115.

[36] R. Gillen, S.J. Clark, J. Robertson, Nature of the electronic band gap in lanthanide oxides, Phys. Rev. B. 87 (2013) 125116. https://doi.org/10.1103/PhysRevB.87.125116.

[37] T. Ogawa, S. Kobayashi, M. Wada, C.A.J. Fisher, A. Kuwabara, T. Kato, M. Yoshiya, S. Kitaoka, H. Moriwake, Isolated energy level in the band gap of Yb2Si2O7 identified by electron energy-loss spectroscopy, Phys. Rev. B. 93 (2016) 201107. https://doi.org/10.1103/PhysRevB.93.201107.

[38] J.P. Perdew, A. Ruzsinszky, G.I. Csonka, O.A. Vydrov, G.E. Scuseria, L.A. Constantin, X. Zhou, K. Burke, Restoring the Density-Gradient Expansion for Exchange in Solids and Surfaces, Phys. Rev. Lett. 100 (2008) 136406. https://doi.org/10.1103/PhysRevLett.100.136406.

[39] G.I. Csonka, J.P. Perdew, A. Ruzsinszky, P.H.T. Philipsen, S. Lebègue, J. Paier, O.A. Vydrov, J.G. Ángyán, Assessing the performance of recent density functionals for bulk solids, Phys. Rev. B. 79 (2009) 155107. https://doi.org/10.1103/PhysRevB.79.155107.

[40] H.J. Monkhorst, J.D. Pack, Special points for Brillouin-zone integrations, Phys. Rev. B. 13 (1976) 5188–5192. https://doi.org/10.1103/PhysRevB.13.5188.

[41] A. Togo, I. Tanaka, First principles phonon calculations in materials science, Scr. Mater. 108 (2015) 1–5. https://doi.org/10.1016/j.scriptamat.2015.07.021.

[42] G. Kresse, J. Furthmüller, J. Hafner, Ab initio Force Constant Approach to Phonon Dispersion Relations of Diamond and Graphite, Europhys. Lett. 32 (1995) 729–734. https://doi.org/10.1209/0295-5075/32/9/005.

[43] K. Parlinski, Z.Q. Li, Y. Kawazoe, First-Principles Determination of the Soft Mode in Cubic ZrO_2, Phys. Rev. Lett. 78 (1997) 4063–4066. https://doi.org/10.1103/PhysRevLett.78.4063.

[44] R. Hultgren, R.L. Orr, P.D. Anderson, K.K. Kelley, Selected values of thermodynamic properties of metals and alloys, American Society of Metals, 1963.

[45] J.B. Mann, Ionization cross sections of the elements calculated from mean-square radii of atomic orbitals, J. Chem. Phys. 46 (1967) 1646–1651. https://doi.org/10.1063/1.1840917.

[46] J.-J. Liang, A. Navrotsky, T. Ludwig, H.J. Seifert, F. Aldinger, Enthalpy of formation of rare-earth silicates Y_2SiO_5 and Yb_2SiO_5 and N-containing Silicate $Y_{10}(SiO_4)_6N_2$, Communications. (1999) 1181–1185.

[47] S. Fujii, A. Ioki, T. Yokoi, M. Yoshiya, Role of phonons on phase stabilization of RE2Si2O7 over wide temperature range (RE = Yb, Gd), J. Eur. Ceram. Soc. 40 (2020) 780–788. https://doi.org/10.1016/j.jeurceramsoc.2019.10.060.

[48] L. Pauling, The nature of the chemical bond. Application of results obtained from the quantum mechanics and from a theory of paramagnetic susceptibility to the structure of molecules, J. Am. Chem. Soc. 53 (1931) 1367–1400. https://doi.org/10.1021/ja01355a027.

[49] A. Louis Allred, Electronegativity values from thermochemical data, J. Inorg. Nucl. Chem. 17 (1961) 215–221. https://doi.org/10.1021/jp020500+.

[50] Y. Kanke, A. Navrotsky, A Calorimetric Study of the Lanthanide Aluminum Oxides and the Lanthanide Gallium Oxides: Stability of the Perovskites and the Garnets, J. Solid State Chem. 141 (1998) 424–436. https://doi.org/10.1006/jssc.1998.7969.

[51] M. Ridley, J. Gaskins, P. Hopkins, E. Opila, Tailoring thermal properties of multi-component rare earth monosilicates, Acta Mater. 195 (2020) 698–707. https://doi.org/10.1016/j.actamat.2020.06.012.

[52] D. Yamamoto, S. Tachibana, Water Vapor Pressure Dependence of Crystallization Kinetics of Amorphous Forsterite, ACS Earth Sp. Chem. 2 (2018) 778–786. https://doi.org/10.1021/acsearthspacechem.8b00047.

[53] M.A. Velbel, Bond strength and the relative weathering rates of simple orthosilicates, Am. J. Sci. 299 (1999) 679–696. https://doi.org/10.2475/ajs.299.7-9.679.

[54] Y. Zhang, Thermodynamic Properties of Rare Earth Sesquioxides, (2016).

[55] C.W. Bale, E. Bélisle, P. Chartrand, S.A. Decterov, G. Eriksson, A.E. Gheribi, K. Hack, I.H. Jung, Y.B. Kang, J. Melançon, A.D. Pelton, S. Petersen, C. Robelin, J. Sangster, P. Spencer, M.A. Van Ende, FactSage thermochemical software and databases, 2010-2016, Calphad Comput. Coupling Phase Diagrams Thermochem. 54 (2016) 35–53. https://doi.org/10.1016/j.calphad.2016.05.002.

[56] R.J.M. Konings, O. Beneš, A. Kovács, D. Manara, D. Sedmidubskỳ, L. Gorokhov, V.S. Iorish, V. Yungman, E. Shenyavskaya, E. Osina, The Thermodynamic Properties of the f-Elements and their Compounds: Part 2. The Lanthanide and Actinide Oxides, J. Phys. Chem. Ref. Data. 43 (2014). https://doi.org/10.1063/1.4825256.

Supplemental Table 1: Ion intensities and related standard uncertainties for Region (1) and Au. A movable shutter is used to interrupt the molecular beam to measure the contents of the Knudsen cell (open) and the background (closed). The true SiO signal is the difference between the open and closed positions.u is 1 standard uncertainty.

Region (1): Lu_2O_3 – Lu_2SiO_5 – Ta

		SiO open		SiO closed	
T [K]	**u**	**Avg. Ion intensity**	**u**	**Avg. Ion intensity**	**u**
1503.2	0.17	2415.3	16.0	187.0	10.5
1503.2	0.17	2524.7	16.6	230.7	5.4
1529.8	0.03	5088.7	23.2	510.0	9.0
1529.8	0.03	5119.8	25.3	578.3	14.1
1535.4	0.08	5462.2	46.4	334.5	12.7
1535.4	0.08	5504.0	26.5	420.7	14.2
1562.7	0.08	10188.0	103.4	944.2	12.7
1562.7	0.08	9820.8	37.2	944.0	8.4
1590.8	0.02	15841.0	100.4	492.8	21.7
1590.8	0.02	15462.2	113.0	918.7	38.6

Au cell

		Au open	
T [K]	**u**	**Avg. Ion intensity**	**u**
1503.2	0.17	27150.3	346.6
1529.8	0.03	40870.0	407.6
1535.4	0.08	47842.0	212.8
1562.7	0.08	73290.2	466.8
1590.8	0.02	118671.8	670.5

Supplemental Table 2: Calculation of pressure and activity for Region (1) from the measured ion intensity and Factsage (FS) SiO pressures. SiO pressure calculated from $P = \frac{kIT}{\sigma}$ where *k* = 1.0E-14 ± 5E-16 and σ = 4.42 ± 0.8. u is 1 standard uncertainty. us for FS vapor pressure are derived from JANAF tables [Chase, JANAF Thermochemical tables, 1998]

T [K]	u	Calc. SiO P [bar]	u	FS SiO P [bar]	u	Activity (a)	u
1503.2	0.17	7.58E-09	1.42E-09	1.41E-05	2.82E-07	5.36E-04	1.02E-04
1503.2	0.17	7.80E-09	1.47E-09	1.41E-05	2.82E-07	5.51E-04	1.05E-04
1529.8	0.03	1.58E-08	2.98E-09	2.45E-05	4.90E-07	6.47E-04	1.22E-04
1529.8	0.03	1.57E-08	2.95E-09	2.45E-05	4.90E-07	6.42E-04	1.21E-04
1535.4	0.08	1.78E-08	3.35E-09	2.74E-05	5.48E-07	6.50E-04	1.23E-04
1535.4	0.08	1.77E-08	3.32E-09	2.74E-05	5.48E-07	6.44E-04	1.22E-04
1562.7	0.08	3.27E-08	6.15E-09	4.69E-05	9.38E-07	6.96E-04	1.32E-04
1562.7	0.08	3.14E-08	5.89E-09	4.69E-05	9.38E-07	6.69E-04	1.26E-04
1590.8	0.02	5.52E-08	1.04E-08	8.01E-05	1.60E-06	6.90E-04	1.30E-04
1590.8	0.02	5.23E-08	9.84E-09	8.01E-05	1.60E-06	6.54E-04	1.24E-04

Supplemental Table 3: Ion intensities and related standard uncertainties for Region (2). A movable shutter is used to interrupt the molecular beam to measure the contents of the Knudsen cell (open) and the background (closed). The true SiO signal is the difference between the open and closed positions. u is 1 standard uncertainty. Activity is calculated using the equation $a\left(SiO_{2,comp}\right)=\left\{\frac{\left[I\left(SiO\right)\right]^3 I\left[MoO_3\right]}{\left[I^{\circ}\left(SiO\right)\right]^3 I^{\circ}\left[MoO_3\right]}\right\}^{0.33}$

Region (2): Lu_2SiO_5 – $Lu_2Si_2O_7$ – Mo

		SiO open		SiO closed		MoO_3 open	
T [K]	**u**	**Avg. Ion intensity**	**u**	**Avg. Ion intensity**	**u**	**Avg. Ion intensity**	**u**
1657.9	0.18	8023.0	38.4	2278.7	30.8	179.8	3.8
1683.4	0.02	13687.0	46.4	3513.5	19.6	273.8	6.8
1703.9	0.05	16769.7	57.2	4023.2	40.0	340.8	11.0
1716.4	0.06	20910.5	61.8	4632.0	33.6	500.5	8.2
1730.8	0.10	26900.7	40.2	5983.5	31.2	690.0	9.5
1754.2	0.19	37389.8	64.4	7928.7	54.8	1044.2	9.9

SiO_2 – Mo reference cell

		SiO open		SiO closed		MoO_3 open	
T [K]	**St.u**	**Avg. Ion intensity**	**u**	**Avg. Ion intensity**	**u**	**Avg. Ion intensity**	**u**
1657.9	0.18	20782.2	46.4	2256.8	12.2	760.7	7.9
1683.4	0.02	33255.7	83.4	3366.8	28.2	1289.3	8.8
1703.9	0.05	41328.3	160.9	4023.2	40.0	1697.5	15.6
1716.4	0.06	50970.5	152.6	4632.0	33.6	2390.5	20.7
1730.8	0.10	71177.0	88.6	5983.5	31.2	3265.8	21.8
1754.2	0.19	100479.5	212.8	7928.7	54.8	4836.7	27.6

Calculation of activity from ratios of ion intensities

T [K]	u	Activity SiO_2	u
1657.9	0.18	0.192	2.28E-03
1683.4	0.02	0.203	2.10E-03
1703.9	0.05	0.200	2.65E-03
1716.4	0.06	0.209	2.22E-03
1730.8	0.10	0.191	1.57E-03
1754.2	0.19	0.191	1.34E-03